Powder Technology 246 (2013) 419–433

Contents lists available at SciVerse ScienceDirect

Powder Technology

journal homepage: www.elsevier.com/locate/powtec

Process control for the synthesis of ZrO_2 nanoparticles using FSP at high production rate

H. Torabmostaedi [a], T. Zhang [a,*], P. Foot [a], S. Dembele [a], C. Fernandez [b]

[a] Faculty of Science, Engineering and Computing, Kingston University, London, SW15 3DW, United Kingdom
[b] Technological Centre Lurederra, Los Arcos, Spain

ARTICLE INFO

Article history:
Received 1 December 2012
Received in revised form 30 April 2013
Accepted 3 May 2013
Available online 10 May 2013

Keywords:
Zirconia nanoparticle synthesis
Flame Spray Pyrolysis
Scale-up
Particle dynamics
Computational fluid dynamics

ABSTRACT

A numerical method of combining CFD with the particle dynamics was developed to study the effect of processing parameters on the formation of nanoparticles by Flame Spray Pyrolysis for up scaling the synthesis of zirconia nanoparticles. This investigation employed a commercial CFD code to simulate the gas flow field and droplet dynamics while three numerical models were developed to predict dynamic viscosity and surface tension of precursor solutions, the sauter mean diameter (SMD) of droplets during atomization and the particle growth inside the flame by coagulation and sintering. The simulation results were compared with experimental data available in this study and literature. The validated models were used to predict the effect of processing parameters, in particular, the effect of pressure drop, sheath gas, oxidant/mixture volume feed ratio (VFR), production rate and precursor concentration on flame dynamics and particle growth. The results show that increasing pressure drop and VFR will be able to decrease the residence time and sintering of nanoparticles in the flame. The variation of inlet sheath gas feeding had a negligible effect on the fluid flow and final particle size. The results also showed that by keeping the VFR and pressure drop at a fixed predicted value, similar particle size can be achieved at higher production rates using fixed precursor concentration.

1. Introduction

Zirconia nanoparticles of characteristic length less than 20 nm have a large potential for industrial applications. Along with high strength and toughness, zirconia also possesses good hardness, wear resistance and thermal shock resistance [1]. These properties have led to the use of zirconia-based components in a number of engineering applications. In addition to their extensive use as gas sensors [2], they are also used in interferometric filters [3], solid oxide fuel cells [4], catalysts [5], thermal barrier coating [6], as well as in dental ceramics [7]. The properties of nanomaterials are extremely dependent on the synthesis method as well as on the processing route; therefore, it is quite important to select the most appropriate technique for preparation of nanomaterials with desired chemical purity, phase and morphology. This challenge is more increased by the necessity to produce them in large amounts while keeping the cost to the minimum. Various techniques, including liquid phase synthesis such as sol gel process [8], gas phase (aerosol) synthesis (chemical vapor synthesis (CVS) [9], and Flame Spray Pyrolysis [10–13]) have been the most commonly used routes for the synthesis of zirconia nanopowders. The aerosol synthesis is quite attractive compared to liquid phase synthesis since it is a one step process and doesn't require several sequential steps to form nanoparticles [14,15]. Flame Spray Pyrolysis (FSP) has become one of the best aerosol synthesis techniques, since both organic and inorganic precursors can be used to produce nanoparticles [16]. This method has many advantages over the other methods as it is low-cost, easy to control particle size, simple processing, high production yield, and easy to convert to mass manufacturing [17]. Fig. 1 shows the schematic of Flame Spray Pyrolysis. Liquid solution containing precursor and fuel is fed into a capillary tube and dispersed by the oxidant. The initial size of droplets depends on many parameters including nozzle geometry, oxidant and solution flow rates, solution properties and relative velocity of solution and oxidant. Heine and Pratsinis [12] calculated the droplet lifetime at different initial droplet sizes based on the temperature and velocity profiles reported by Mueller et al. [10] and Heine and Pratsinis [12]. Droplet life time and traveling distance increased significantly as the initial droplet size increased. Larger droplets can even escape from the flame which may cause hollow particles [18]; therefore, good care must be taken to achieve small droplets with uniform distribution. After atomization, the solution is ignited by using a small methane–oxygen pilot flame which is positioned around the nozzle tip. In FSP the energy of the flame is used to drive chemical reaction of the precursor to produce clusters which quickly grow into nanoparticles by coagulation and sintering. The primary particle size and degree of agglomeration are very important indexes for final product performance which will be determined by the properties of the flame [16]. The extent of aggregation of primary particles can be distinguished by the strength of the forces that hold them together. These aggregates can either be held together by strong chemical or sintering bonds (hard-agglomerates; formed

* Corresponding author.
E-mail address: t.zhang@kingston.ac.uk (T. Zhang).

0032-5910/$ – see front matter.
http://dx.doi.org/10.1016/j.powtec.2013.05.006

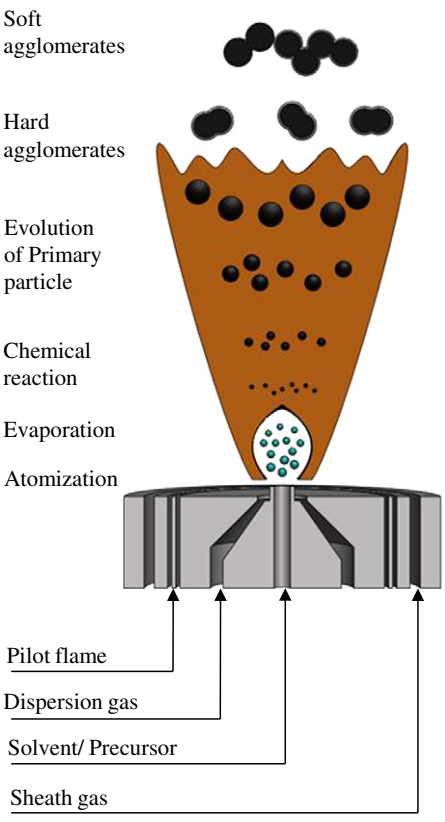

Fig. 1. Schematic of FSP apparatus.

at intermediate temperature) or bonded by weak physical van der Waals forces (soft-agglomerates; formed once sintering and growth of primary particle diameter stops). Tsantilis and Pratsinis [19] identified the regions of soft-, hard- and non-agglomerate silica particles in the high temperature flames on the basis of particle sintering and coalescence. The region of hard agglomerates is defined at the point where collision aggregate diameter/primary particle diameter, d_c/d_p is equal to 1.01 while the transition from hard to soft agglomerates is defined at the point where the primary particle diameter has reached 99% of its final d_p. Grohn et al. [20,21] defined the transition point at 95% of the final d_p to compensate the fluctuation of his numerical accuracy. The design of FSP systems is complex because the mixture of precursor and fuels needs to be atomized and efficient combustion is so difficult to achieve due to the variation of liquid properties which have a direct effect on the size and properties of nanoparticles. Advanced computational models have been developed to gain an insight to the FSP process. Most of the studies have been focused on particle modeling based on experimental data [10–13] and only one single numerical investigation reported on the lab scale production (14.8 and 29.6 g/h) without investigating the process parameters [21]. The properties of the nanoparticles in FSP depend on so many parameters, such as nozzle design, droplet size and lifetime, temperature, velocity and oxidant content. The design of the FSP nozzle and its parameters is therefore critical in order to up-scale the production. In this study, investigation is performed to examine the effect of process parameters on the growth of zirconia particles. A commercial CFD code, ANSYS FLUENT was used to solve the multicomponent droplet evaporation, combustion and gas flow field in FSP. The CFD code is coupled with an in-house Fortran code which is developed based on the Kruis et al. [22] model to simulate the particle growth during FSP. The employed mathematical models have been strongly tested against experimental data. The prediction of gas dynamics, initial droplet size and primary particle diameter in FSP process were validated against the documented experimental measurement [10–13]. The aim of the present study is to optimize the FSP process in order to have a controlled scaling up at higher production.

2. Liquid properties and composition

The solution used in this study was the mixture of zirconium n-propoxide (ZnP, Alfa Aesar, 70 wt.% in n-propanol) diluted in Ethanol (ethanol, ReAgents, >99.8%) resulting in precursor solutions of 0.5, 1, 1.5, 2 and 2.23 M ZnP. The viscosity of the solutions was determined with a Brookfield viscometer (LVDV-II-Pro) operated with an Ultra Low (UL) adapter to allow low viscosity measurement (down to 1 mPa s). The viscometer closed chamber tube was immersed in a Fisher Scientific water bath which could control the temperature from 0 to 100 °C. The viscometer was calibrated with the calibration fluid provided by Brookfield Engineering Laboratories at 25 °C. The viscosities were measured at different applied torques ranging between 10 and 100%. All the measurements were performed three times under steady state conditions. The reproducibility in measurement was within 2%. The surface tension of precursor solutions was measured by the Du Nouy ring method, using a Sigma 703 surface tensiometer at 25 °C. The tensiometer was calibrated with distilled water before each use. Surface tension was measured three times at each concentration, and the degree of reproducibility was within 0.1 mN/m.

3. Theoretical model

In this study, Eulerian approach was used to treat the continuous phase using Shear Stress Transport (SST) k–ω model [23] for turbulence description. The droplet flow field was modeled using DPM Lagrangian formulation by following discrete trajectories of droplets defined according to initial position, size and velocities. A monodisperse model was developed to predict the evolution of nanoparticles based on a detailed calculation of species concentration, density, velocity and temperature within the flame.

3.1. Gas dynamics

The continuous phase is assumed to be an ideal gas and as illustrated in Fig. 2, the FSP configuration has an axisymmetric geometry and a two dimensional model is employed to reduce the complexity and computational time. The governing equations for the 2-D model in the Cartesian tensor form are:

– Mass conservation equation

$$\frac{\partial \rho}{\partial t} + \frac{\partial}{\partial x_j}\left(\rho u_j\right) = 0 \tag{1}$$

– Momentum conservation

$$\frac{\partial}{\partial t}(\rho u_i) + \frac{\partial}{\partial x_j}\left(\rho u_i u_j\right) = -\frac{\partial p}{\partial x_i} + \frac{\partial \left(\tau_{ij}\right)_{eff}}{\partial x_j} + \frac{\partial}{\partial x_j}\left(-\rho \overline{u'_i u'_j}\right) \tag{2}$$

where $-\rho\overline{u'_i u'_j}$ is the Reynolds stress, which represents the effect of turbulent fluctuation on the fluid flow.

– Energy transport equation

$$\frac{\partial}{\partial t}(\rho E) + \frac{\partial}{\partial x_i}\left[u_i(\rho E + p)\right] = \frac{\partial}{\partial x_j}\left(k_{eff}\frac{\partial T}{\partial x_j} - \sum_j e_j J_j + u_i\left(\tau_{ij}\right)\right) + S_h. \tag{3}$$

Fluid in turbulent reacting flows is often considered as Newtonian and hence the shear stress can be related to velocity gradient.

$$\left(\tau_{ij}\right)_{eff} = \mu_{eff}\left(\frac{\partial u_i}{\partial x_j} + \frac{\partial u_j}{\partial x_i}\right) - \frac{2}{3}\mu_{eff}\frac{\partial u_k}{\partial x_k}\delta_{ij} \tag{4}$$

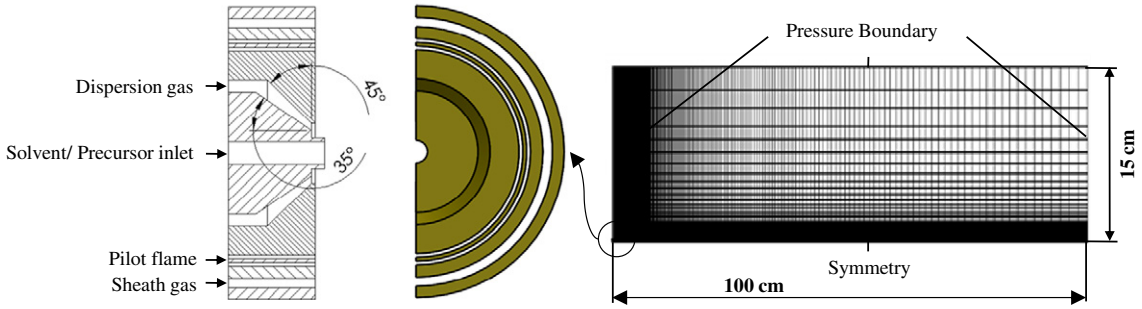

Fig. 2. Nozzle geometry and computational domain.

– Species conservation

$$\frac{\partial}{\partial t}(\rho Y_i)+\frac{\partial}{\partial x_i}(\rho u_i Y_i)=\frac{\partial}{\partial x_i}\left(\frac{\mu_t}{Sc_t}\frac{\partial Y_i}{\partial x_i}\right)+R_F \tag{5}$$

where R_F is the time mean reaction rate and Sc_t is the Schmidt number set equal to 0.7. The term between the brackets on the right hand side of Eq. (3) consists of energy transfer due to conduction, species diffusion and viscous dissipation, respectively. S_h is the heat source due to the chemical reaction or radiation. The Discrete Ordinates (DO) model [24] is incorporated in the enthalpy balance to account not only for scattering but also for the exchange of radiation between gas and droplets. In the DO model, the radiative transfer equation (RTE) for an absorbing, emitting, and scattering medium at position $\vec{r}$ in the direction $\vec{s}$ is given by

$$\nabla\left(I\left(\vec{r},\vec{s}\right)\vec{s}\right)+(a+\sigma_s)I\left(\vec{r},\vec{s}\right)=an^2\frac{\sigma T^4}{\pi}+\frac{\sigma_s}{4\pi}\int_0^{4\pi}I\left(\vec{r}\,\vec{s}'\right)\Phi\left(\vec{s},\vec{s}'\right)d\Omega' \tag{6}$$

where I is the radiation intensity and it depends on position $\vec{r}$ and direction $\vec{s}$.

– Turbulence kinetic energy

$$\frac{\partial}{\partial t}(\rho k)+\frac{\partial}{\partial x_i}(\rho k u_i)=\frac{\partial}{\partial x_j}\left(\mu+\frac{\mu_t}{\sigma_k}\frac{\partial k}{\partial x_j}\right)+\tilde{G}_k-Y_k \tag{7}$$

– Dissipation rate of turbulence kinetic energy

$$\frac{\partial}{\partial t}(\rho\omega)+\frac{\partial}{\partial x_i}(\rho\omega u_i)=\frac{\partial}{\partial x_j}\left(\mu+\frac{\mu_t}{\sigma_\omega}\frac{\partial \omega}{\partial x_j}\right)+G_\omega-Y_\omega+D_\omega \tag{8}$$

where turbulent viscosity is defined as

$$\mu_t=\frac{\rho k}{\omega}\frac{1}{max\left[\frac{1}{\alpha^*},\frac{\vartheta F_2}{a_1\omega}\right]}. \tag{9}$$

In these equations, $\tilde{G}_k$ represents the generation of turbulence kinetic energy due to mean velocity gradients, G_ω represents the generation of ω, Y_k and Y_ω represent the dissipation of k and ω due to turbulence, and D_ω represents the cross-diffusion term. The flame combustion was modeled by using a single step reaction mechanism. The complete stoichiometric combustion reactions can be expressed as:

Ziconium n – propoxide :	$C_{12}H_{28}O_4Zr+18O_2=ZrO_2+12CO_2+14H_2O$
1 – Propanol :	$C_3H_8O+4.5O_2=3CO_2+4H_2O$
Ethanol :	$C_2H_6O+3O_2=2CO_2+3H_2O$
Methane :	$CH_4+2O_2=CO_2+2H_2O$.

The rate of fuel combustion is calculated using the eddy-dissipation model [25]. Since most fuels are fast burning, the overall rate of reaction is controlled by turbulent mixing instead of calculation of Arrhenius chemical kinetics. The reaction rate of species F was calculated as the smallest of the turbulent dissipation rates of F, O and P [25]:

$$R_F=-A\rho\omega min\left[Y_F,\frac{Y_O}{f},B\frac{Y_P}{1+f}\right] \tag{10}$$

where A and B are the dimensionless empirical coefficients with default values of 4 and 0.5, respectively. In Eq. (10), Y is the mass fraction of fuel (F), oxidant (O), and products (P) and f is the stoichiometric mass requirement of oxidant to consume 1 kg of fuel.

3.2. Droplet transport model

The discrete phase droplet trajectories are computed by integrating the force balance equation. This equation has terms for the drag force and the gravity force and there are also numerous additional forces that can be included. Typically for combustion applications the drag and gravity forces are the main influences on particle trajectories. The droplet may exchange mass, momentum and heat with the gas phase and that occurs within the control volumes that are crossed by the droplet trajectory. The trajectory is calculated by integrating the droplet force balance equation:

$$\frac{du_d}{dt}=\frac{18\mu}{\rho_d d_d^2}\frac{C_D Re}{24}(u-u_d)+g_i\left(1-\frac{1}{B}\right) \tag{11}$$

where B is droplet to gas density ratio, u is the gas velocity, u_d is the droplet velocity, and ρ_d is the density of the droplet. The drag coefficient is defined as

$$C_D=b_1+\frac{b_2}{Re}+\frac{b_3}{Re^2} \tag{12}$$

where b_1, b_2 and b_3 are constants that apply for spherical droplets over wide ranges of Re, as provided by Morsi and Alexander [26]. The interaction of eddies with the droplets is included through the Discrete Random Walk (DRW) model [27,28]. The initial droplet size is calculated by using a correlation which was derived by Elkotb et al. [29] for external-mixing nozzles as follows

$$\mathrm{SMD}=Cd_0\mathrm{Re}^{-0.39}\mathrm{We}^{-0.18}\left(\frac{\dot{m}_{mix}}{\dot{m}_g}\right)^{0.29} \tag{13}$$

where

$$Re=\frac{\rho_{mix}d_0\left(u_g-u_{mix}\right)}{\mu_{mix}},\quad We=\frac{\rho_{mix}d_0\left(u_g-u_{mix}\right)}{\gamma_{mix}} \tag{14}$$

where μ_{mix} and γ_{mix} are the viscosity and surface tension of the precursor solution at different concentrations. The scaling constant, C, was changed from 51 [29] to 45 as it was found to be the best point to validate the measured data [13] for the current geometry at cold gas simulation. Gas velocity u_g at the nozzle exit is obtained from the solution of momentum equation in CFD code. The liquid velocity is given by

$$u_l = \frac{\dot{m}_{mix}}{\rho_{mix} A_0} \tag{15}$$

where A_0 is the cross section area of the liquid exit. Mixture density was calculated by

$$\rho_{mix} = \frac{1}{\sum_{i=1}^{n} \frac{Y_i}{\rho_{l_i}}} \tag{16}$$

where Y_i and ρ_{l_i} are the mass fraction and density of component i, respectively. Several semi-empirical relations were used to find the best relation for correlating the dynamic viscosity and surface tension of liquid mixtures based on the pure-components data. The single parameter equation of Grunberg and Nissan [30] is given as

$$A_{mix} = \exp(x_1 \ln A_1 + x_2 \ln A_2 + x_1 x_2 G) \tag{17}$$

where x_1 and x_2 are the mole fractions of components 1 and 2. Tamura and Kurata [31] proposed the following equation:

$$A_{mix} = x_1 V_1 A_1 + x_2 V_2 A_2 + 2(x_1 x_2 V_1 V_2)^{\frac{1}{2}} C \tag{18}$$

where V_1 and V_2 are the volume fractions of components 1 and 2. Later on, Hind et al. [32] derived the following equation:

$$A_{mix} = x_1^2 A_1 + x_2^2 A_2 + 2 x_1 x_2 D \tag{19}$$

where the parameter A can be substituted by both viscosity μ and surface tension γ. The constants G, C and D are regarded as a measure of the strength of the molecular interactions between the mixing components which is dependent on temperature but independent of composition. In this work, subscript 1 refers to ZnP, whereas subscript 2 refers to the ethanol. The correlating ability of Eqs. (17)–(19) was tested by calculating the standard percentage deviations σ_d (%) between the measured and calculated values as follows [33]

$$\sigma_d(\%) = \left[\frac{1}{n-k} \sum \left\{ \frac{100\left(y_{\exp} - y_{cal}\right)}{y_{\exp}} \right\}^2 \right]^{\frac{1}{2}} \tag{23}$$

where n and k represent the number of data points and numerical coefficients, respectively, and $y_{\exp}$ and y_{cal} refer to measured and calculated viscosity μ_{mix} and surface tension γ_{mix} of precursor solutions at different ZnP concentrations.

3.3. Heat and mass transfer model for droplets

Droplet evaporation must be expressed in an accurate and simple manner to be implemented in a CFD code and it has the most important part in simulation of spray combustion because the concentration of fuel vapor is determined by the evaporation rate. To determine the vaporization rate, Nusselt number, and Sherwood number, equations should be solved simultaneously for the temperature and composition at the droplet surface. The energy conservation equation for the droplets is expressed as follows:

$$m_d c_p \dot{T}_d = A_d \varepsilon_d \sigma \left(T_R^4 - T_d^4\right) - \sum_i \dot{m}_i \left(\mathbf{h}_{v,i}\right) + \boldsymbol{h} A_d (T_\infty - T_d) \tag{20}$$

where m_d and A_d are the droplet mass and surface area, c_p is the droplet specific heat, $\mathbf{h}_{v,\,i}$ is the droplet latent heat, and T_∞ and T_d are surrounding gas and droplet temperature. The heat transfer coefficient is defined as

$$\boldsymbol{h} = \frac{k_\infty}{d_d}\left(2 + 0.6 Re_d^{0.5} Pr^{0.33}\right) \tag{21}$$

where k_∞ is the thermal conductivity of surrounding gas, and Pr is Prandtl number. The droplet vaporization rate is estimated for N-component mixture by [34]

$$\sum_{i=1}^{N} \dot{m}_i = A_d M_{w,i} \frac{D_{i,m}}{d_d}\left(2 + 0.6 Re_d^{0.5} Sc^{0.33}\right)\left(C_{i,s} - C_{i,\infty}\right) \tag{22}$$

where $\dot{m}_i$ is the evaporation rate of component i in the droplet, $M_{w,i}$ is the molecular weight of the component i in the droplet mixture, $D_{i,m}$ is the diffusion coefficient, Sc is the Schmidt number, and $C_{i,s}$ and $C_{i,\infty}$ are the concentration of component i on the droplet surface and in the bulk. When the total vapor pressure at the droplet surface exceeds the pressure of the continuum gas, the multicomponent droplets are in the boiling regime and following equation can be used to calculate their evaporation rate [35]

$$\dot{m}_i = x_i \pi d_d \left(\frac{k_\infty}{c_{p\infty}}\right)\left(2 + 0.6 Re_d^{0.5} Pr^{0.33}\right) \ln\left(1 + \frac{c_{p\infty}(T_\infty - T_d)}{h_{v,i}}\right) \tag{26}$$

where k_∞ is the gas thermal conductivity, and $c_{p\infty}$ is the specific heat of the bulk flow. The following assumptions were applied to the modeling of the discrete phase:

- The volume fraction occupied by the discrete phase droplets is less than 10%; thus, the number of collisions between liquid droplets is neglected.
- The droplets do not break up into smaller elements.
- All droplets are identical at the inlet.

3.4. The dynamics of particle growth

The simple monodisperse model of Kruis et al. [22] is used in this study to describe the particle growth of ZrO_2. This model is used due to its simplicity and superior performance for predicting the primary particle diameter in the previous studies [10,36–38]. The model makes the following assumptions:

- Homogeneous nucleation is followed by particle growth through cluster–cluster aggregation with simultaneous coalescence of primary particles
- Initial monomer concentration is obtained after complete decomposition of precursor
- The monomers are regarded as stable initial particles
- The particle growth began after complete evaporation of mixture droplets
- The particles in the flame do not have any effect on the gas flow field.

The rates of change of particle number (N), area (a), and volume (v) concentration are given by

$$\frac{dN}{dt} = \frac{1}{2}\rho\beta N^2 \tag{23}$$

$$\frac{da}{dt} = -\frac{1}{N}\frac{dN}{dt}a - \frac{1_{(a-a_s)}}{t_{\sin}} \tag{24}$$

$$\frac{dv}{dt} = -\frac{1}{N}\frac{dN}{dt}v \tag{25}$$

where N is the number concentration of the aggregates per unit mass of gas and ρ is the gas density. The expressions for surface area of a completely fused (spherical) aggregate a_s and collision frequency function β can be found in Kruis et al. [22]. The characteristic sintering time for two equally sized spheres to coalesce by grain boundary diffusion is given as [39]

$$t_{sin} = \frac{FRTr_p^4}{wD_{gb}\gamma\Omega}. \tag{26}$$

Here $F = 0.013$ is the dimensionless time period constant for the sintering [40], T is the gas temperature which was found from CFD simulation, w is the grain boundary width [41], D_{gb} is the grain boundary diffusion coefficient [42], γ is the surface tension [43] and Ω is the atomic volume of zirconia. The primary particle diameter, d_p, number of primary particles per agglomerate, n_p, and collision aggregate diameter, d_c, are [22]

$$d_p = \frac{6v}{a}, \quad , \quad n_p = \frac{a^3}{36\pi v^2}, \quad d_c = d_p\left(n_p^{\left(\frac{1}{D_f}\right)}\right) \tag{27}$$

where $v_0\left(=\frac{M_{ZrO_2}}{\rho_{ZrO_2}}\times N_A\right)$ is the monomer volume, $a_0\left(=6\times\frac{v_0}{d_{monomer}}\right)$ is the monomer surface area, $d_{monomer}\left(=\left(6\times\frac{v_0}{\pi}\right)^{\frac{1}{3}}\right)$ is the monomer diameter and D_f is the fractal dimension which was set as 1.8, a commonly-used value for aggregates generated in high temperature aerosol processes [22,44]. Ordinary differential Eqs. (23)–(25) can be further transformed as follows:

$$\frac{ds}{dt} = \frac{ds}{dx}\frac{dx}{dt} = \frac{ds}{dx}u_g \qquad \text{where} \qquad S = N, v, a \tag{28}$$

where u_g is the gas velocity at distance x from the CFD code. Eqs. (23)–(25) were solved numerically by using the subroutine VODPK [45] with initial conditions (x = the complete evaporation point of the mixture droplets, which is a function of the process parameters): $N = N_0, v = v_0, a = a_0$, where N_0 is initial monomer concentration of zirconia which was calculated by CFD code as follows:

$$N_0 = \frac{G_{ZrO_2} * 1000}{\rho} * N_A \tag{29}$$

where G_{ZrO_2} (kmol m^{-3}) is the molar concentration of zirconia after complete decomposition of precursor.

4. Numerical method

The configuration of the simulated burner is consistent with the experimental setup [10,11]. The external mixing nozzles enable greater control of atomization by independent control of both liquid and oxidant flows, thus, external mixing nozzles are typically preferred for flame spray processes. The nozzle consists of a capillary tube with a diameter of 0.5 mm for feeding the liquid and an annular gap (x) for atomizing the liquid droplets. The annular gap size depends on the desired pressure drop in the working mass flow rate. There are three more concentric tubes around the atomizing gas inlet. Methane and oxygen were supplied through the first two annuli to form a diffusion flame to ignite the main flame. To improve the ignition of main flame, the diameters of these two annuli are modified according to the work of Heine et al. [12,13]. The last annulus is to provide excess oxygen for the main flame close to the nozzle exit. The solution of 0.5 mol zirconium n-propoxide 70 wt.% in n-propanol diluted in ethanol is injected into a pre-existing methane–oxygen flame. The solvent(s) then evaporates and combusts, representing the precursors to the high temperature flame. At that moment, chemical reactions and particle growth mechanisms will take place to produce zirconia nanoparticles. The axisymmetric FSP apparatus can be well represented by a 2D simulation domain which was adopted in this study, as depicted in Fig. 2. The mesh consists of 640 axial nodes and 120 radial nodes. The grid around the precursor solution and dispersion gas inlet was successively refined in a grid-independent study in order to accurately capture the steep variations in flow properties due to the effects of compressibility of oxidant. A constant pressure condition was used at the outlets of the

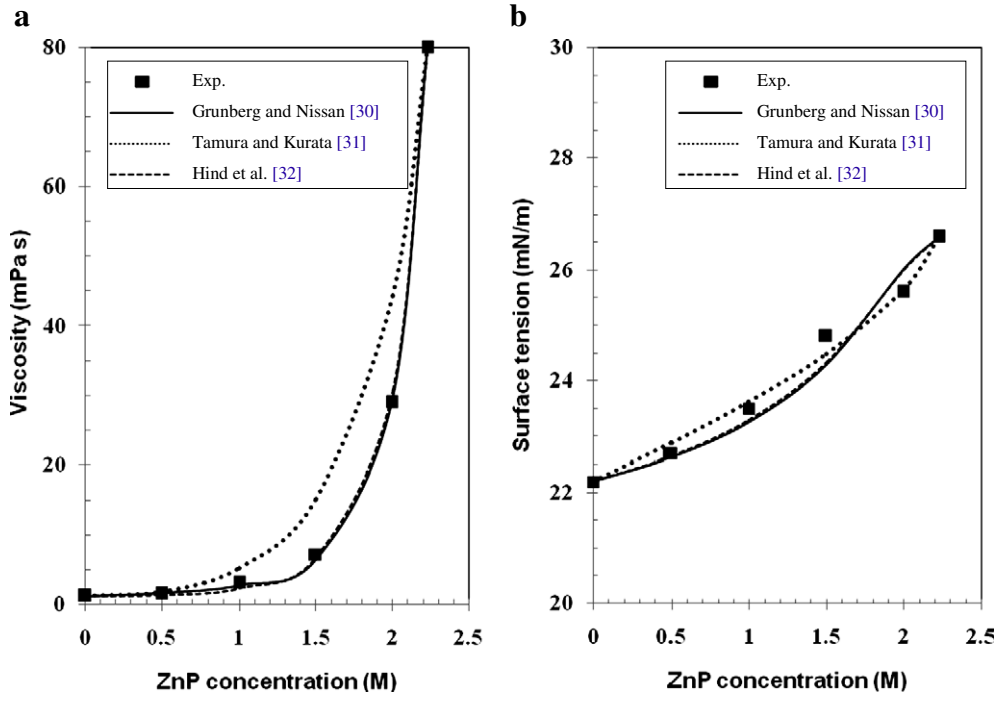

Fig. 3. Average (a) viscosity and (b) surface tension of solution at different precursor concentrations.

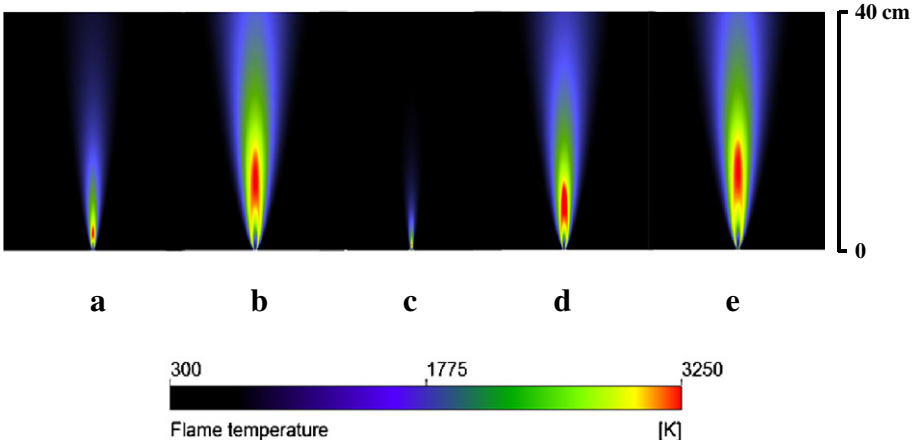

Fig. 4. Temperature distribution of (a) 27.1 ml/min (0.5 M ZnP), (b) 81.1 ml/min (0.5 M ZnP), (c) 6.8 ml/min (1 M ZnP), (d) 54.1 ml/min (1 M ZnP), and (e) 81.1 ml/min (1 M ZnP) at constant sheath and dispersion gas of 15 and 50 l/min, respectively.

outside domain (1 atm). The governing equations for the conservation of mass, momentum, energy, turbulence, chemical species and radiation were solved sequentially by a control volume-based technique. A second-order upwind discretization scheme was used since it ensured the accuracy, stability and convergence. SIMPLEC algorithm (SIMPLE-Consistent) described by Van Doormaal and Raithby [46] was used for pressure–velocity coupling, which uses a relationship between velocity and pressure corrections to enforce mass conservation and to obtain the pressure field. The appropriate under-relaxation factors were imposed to avoid instability in the solution.

5. Results and discussion

5.1. Validation

Fig. 3a shows the average viscosity of precursor solutions as a function of ZnP concentration. The average viscosities of pure ethanol and 0.5 M ZnP in ethanol were 1.2 and 1.54 mPa s which were in a good agreement with literature values of 1.08 [47] and 1.52 mPa s [13], respectively. With increasing ZnP concentration the viscosity increases smoothly and reaches the value 7.22 mPa s at 1.5 M. At higher concentration, the viscosity had a big jump to 29 and 80 mPa s for 2 and 2.23 (pure ZnP solution) M concentrations, respectively. The surface tension data were plotted against the precursor concentration, as shown in Fig. 3b. The average surface tension of pure ethanol increased from 22.2 to 22.7 mN/m when adding 0.5 M ZnP to ethanol. These values were in a good agreement with literature values of 21.82 [48] and 22.56 mPa s [13] for ethanol and 0.5 M ZnP in ethanol, respectively. As the concentration of ZnP in ethanol increases from 0.5 to 2.23 M, the surface tension of the mixture increases continuously from 22.7 to 26.6 mN/m. Applying the measured viscosity data for pure ethanol and ZnP to the correlations of Eqs. (17) and (19) resulted in a good agreement with the measured values at different ZnP concentrations while the mixture viscosity was over predicted when Eq. (18) was used. Despite the over estimation of Eq. (18) in predicting the mixture viscosity, better results were obtained by using this equation to predict the surface tension of mixture liquid compared to the other equations. This can be seen by comparing the standard percentage deviations of these equations for prediction of viscosity and surface tension as well. The average standard percentage deviations of Eqs. (17), (18), and (19) for predicting mixture viscosity were approximately 7.36, 63.53 and 6.56%, while these values reduced to 1.26, 0.73 and 1.14% for predicting the surface tension. Thus, the correlating abilities of Eqs. (19) and (18) were found to be reasonably good for predicting mixture viscosity and surface tension, respectively. In order to predict

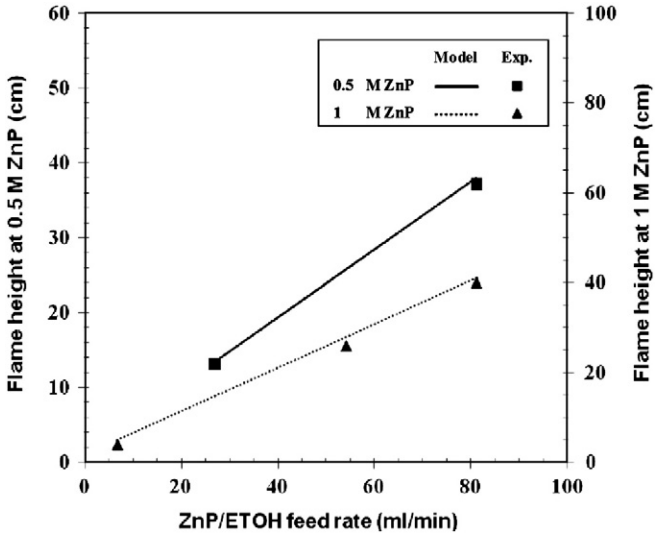

Fig. 5. Comparisons of numerical and experimental data [10,11] for flame height as a function of feed rate at 0.5 and 1 M ZnP concentration in ethanol.

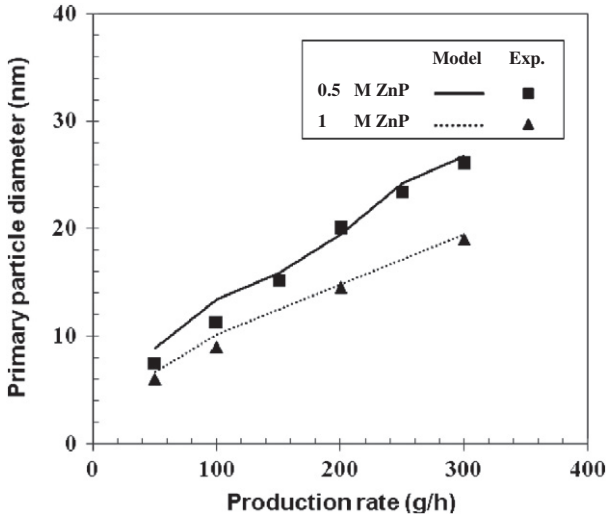

Fig. 6. Comparisons of numerical and experimental data [11] for the primary particle diameter as a function of production rate at 0.5 and 1 M ZnP concentration in ethanol. The sheath and dispersion gas are fixed at 15 and 50 l/min, respectively.

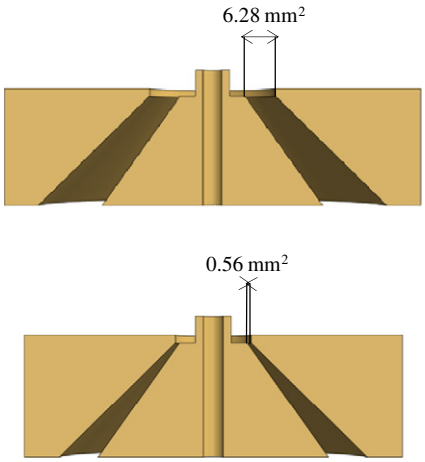

Fig. 7. Nozzle configuration alteration in order to achieve higher applied pressure at constant gas flow rate.

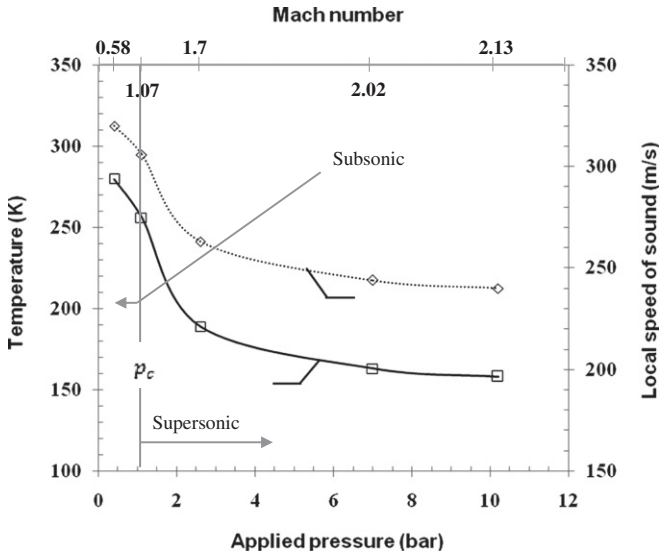

Fig. 8. Effect pressure drop on the temperature and local speed of sound at the expansion region.

the initial droplet size during the atomization in FSP, the correlation of Elkotb et al. [29] was validated by comparing the theoretical and measured [13] values at 0.5 M ZnP/ethanol feed rates of 13.5, 27.1, 54.2 and 81.1 ml/min. Applying these feed rates to Eq. (13) results in predicted initial droplet sizes of 12.8, 15.6, 19.2 and 21.4 which are in good agreement with measured droplet size of 14, 15.4, 19.8 and 21.2, respectively. Fig. 4 shows the temperature distribution of five simulated flames at feed rates of 27.1 and 81.1 ml/min (0.5 M ZnP concentration) and 6.8, 54.1 and 81.1 ml/min (1 M ZnP concentration). The temperature profiles of flames are strongly influenced by the combustion, which depends on the availability of fuel and oxygen. It can be seen that the high temperature zone of the flame moves away from the burner exit as solution feed rates increase. This is a direct result of the increase in supplied fuel energy and lack of supplied oxidant at the nozzle exit. The numerical and measured [10] data for the flame height (calculated as axial position where the temperature reduced to 1500 K, [10]) as a function of solution feed rate at two ZnP concentration are plotted in Fig. 5. Increasing the solution feed rate increased the supplied fuel energy to the flame which resulted in higher flame height. Comparing the flame height at 0.5 and 1 M ZnP in ethanol, good agreement was found between the numerical and measured values [10,11]. The flame height increased from 38 to 41 cm when the precursor concentration doubled at the same solution feed rate (81.1 ml/min). Increasing the precursor concentration from 0.5 to 1 M resulted in higher enthalpy content for the flame, prolonged the combustion and increased the flame height. Fig. 6 shows the comparison between numerical and measured [11] BET-equivalent average diameter of the zirconia primary particles as a function of production rate at 0.5 and 1 M precursor concentration. The numerical zirconia diameters are in good agreement with measured BET-equivalent average diameter. Increasing the production rate from 50 to 300 g/h increases the primary zirconia particle diameter from 8.9 to 26.7 nm (solution feed rates are from 13.5 to 81.1 ml/min at 0.5 M ZnP), and from 6.7 to 19.4 nm (solution feed rates are from 6.8 to 40.55 ml/min at 1 M ZnP) while the measured values are 7.5 to 26 nm (0.5 M ZnP), and 6 to 19 (1 M ZnP), respectively. The validated models were then used to investigate the effects of processing parameters in this study.

Table 1
Definition of the starting variables and fundamental quantities used for the analysis of the pressure drop.

Case	1	2	3	4	5
Atomizing gap area (mm^2)	6.28	3.45	1.88	0.8	0.56
Pressure drop (bar)	0.4	1.1	2.6	7	10.2
Atomizing angles	35, 45°				
ZnP/ethanol feed rate (ml/min)	81.1				
Dispersion gas flow rate (l/min)	70				
Zirconia production (g/h)	300				

5.2. Effect of processing parameters

In FSP process, the physical and chemical properties of nanoparticles are dependent on a large number of parameters, such as the dispersion gas velocity, nozzle design, entraining gas, dispersion gas/mixture feeding ratio, and fuel and precursor properties and their concentration. To improve the phase, size and morphology of the nanoparticles, it is necessary to optimize all of the relevant experimental parameters. In this study, the effects of pressure drop across the dispersion gas exit, sheath gas flow rate, Gas to Liquid Flow Ratio (GLFR), production rate and the concentration of oxide precursor were thoroughly analyzed.

5.2.1. Effect of pressure drop

The effect of pressure drop on flame structure and particle size during FSP was investigated using a solution of 0.5 mol ZnP in ethanol

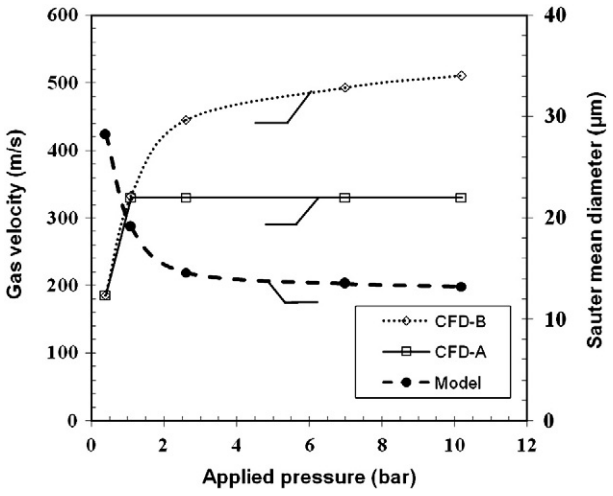

Fig. 9. Simulated gas velocity at the nozzle throat (CFD-A) and after expansion (CFD-B), and calculated initial droplet size (based on the velocity data in the expansion region) at different applied pressures.

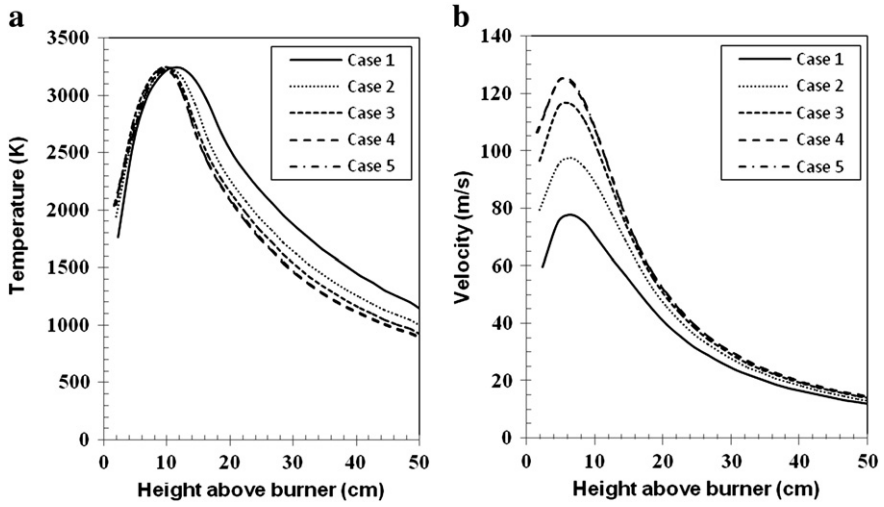

Fig. 10. Variation of (a) centerline temperature and (b) velocity profiles at different applied pressures.

by keeping the mass flow rate of precursor and dispersion gas constant. Increasing the applied pressure at constant liquid and gas flow rate was performed by decreasing the dispersion gas gap size (see Fig. 7). Series of cases were defined in order to vary the applied pressure from 0.4 up to 10.2 bar (Table 1). This was achieved by decreasing the cross section area of the nozzle throat from 6.28 to 0.56 mm^2 for 0.4 and 10.2 bar, respectively. The flow regime in the nozzle throat depends on the nozzle configuration. Our nozzle has a convergent–divergent configuration which means the maximum gas velocity in the throat cannot be more than 330 m/s (sonic regime) but depends on the pressure drop, velocity can increase in the diverging section at the throat exit and expands to supersonic flow. Fig. 8 shows the critical pressure (Mach number equal to 1), at which the transition from subsonic to sonic flow occurs. After critical point, the flow in the nozzle throat is sonic for all case studies which mean the Mach number is equal to one in the throat. At the throat exit, the nozzle configuration diverges and the flow is expanded to a supersonic Mach number that depends on the area ratio (AR) of the exit to the throat. Since the mass flow is kept constant, increasing the (AR) by decreasing the throat gap size will increase the pressure drop and expansion at the throat exit which lowers the exit temperature and local speed of sound. This behavior can be seen from Fig. 8, which shows the exit temperature, local speed of sound and Mach number as a function of applied pressure. Increasing the pressure drop from 0.4 to 10.2 bar reduced the exit temperature and local speed of sound from 280 to 155 K and from 320 to 240 m/s while the Mach number is increased from 0.58 to 2.13, respectively. Fig. 9 shows the gas velocity at the throat and after expansion. The gas velocity at the throat will increase steadily until it reaches its sonic value at ~1.1 bar pressure drop. After this point, the velocity at the throat is constant at 330 m/s but in the expansion region, it increases steadily to 510 m/s at 10.2 bar pressure drop. For external-mixing air-assist atomizers, the relative velocity between the liquid and atomization gas is a key factor governing atomization quality [49]. As the applied pressure of the atomizing gas increases, the SMD value decreases. Fig. 9 also demonstrates the dependence of the calculated droplet diameter on the gas applied pressure and exit velocity at constant value of gas and liquid feed rate (70 l/min, 81.1 ml/min). At 0.4 bar pressure drop, the SMD value was found to be equal to 28.3 μm, whereas this value decreased to 13.2 μm at 10.2 bar. This shows the strong

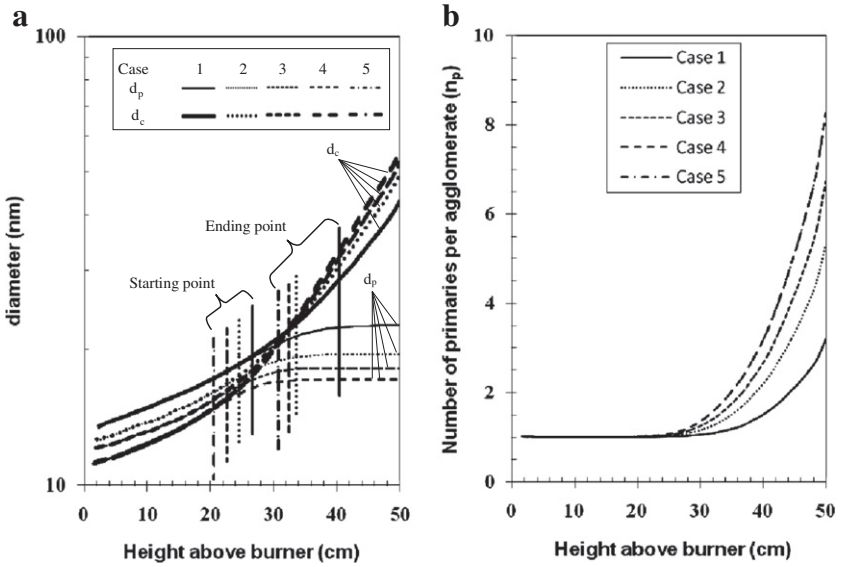

Fig. 11. Evolution of zirconia (a) primary particle diameter (d_p) and agglomerate collision diameter (d_c), and (b) number of primary particles per agglomerate predicted by the proposed model at different pressure drops. The vertical lines represent regions of formation of hard agglomerates at each case study.

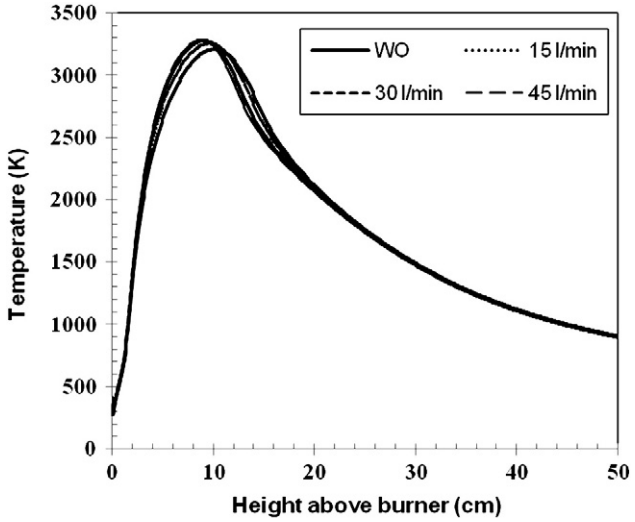

Fig. 12. Centerline flame temperatures at above the burner for oxygen and ZnP/ethanol flow rates of 70 l/min and 81.1 ml/min (Case 4) at different sheath gas flow rates.

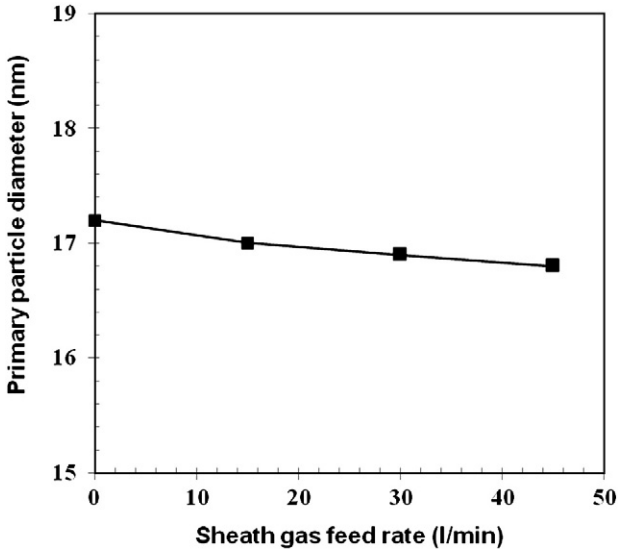

Fig. 14. Effect of the sheath gas feed rate on the predicted primary particle diameters.

dependence of the droplet diameter on the gas applied pressure. Fig. 10 shows the calculated centerline flame temperatures and velocities at variable pressure drop across the nozzle tip for various gap sizes of dispersion. The temperature in all cases increases rapidly at initially stage and decreases slowly when the distance from nozzle exit is increased after reaching the maximum temperature of about 3250 K. The results show that increasing the applied pressure of dispersion gas from 0.4 to 10.2 bar increases the quenching rate and consequently decreases the flame height. The flame height decreased from 39 to 29 cm for case 1 and 5, respectively. This is a direct result of the increase of oxygen availability to the reaction zone which intensifies the mixing of fuel and oxygen at the burner exit and the reduction of droplet size due to the increase of gas/liquid relative velocity which was discussed earlier. Since the gas flow rate was kept constant, the dispersion velocity at the nozzle exit was proportion to the pressure drop across the nozzle. The peak velocity increased from 78 to 124 m/s when the pressure drop was increased from 0.4 (case 1) to 7 bar (case 4) while the latter increased by only 1 m/s at 10.2 bar (case 5) pressure drop. Flame gas velocity determines the residence time of the primary particles in the flame. The higher is the flame velocity, the lower is the residence time for particles in high temperature zone, which will lead to lower growth of primary particle size. Fig. 11a shows the evolution of primary particle (thin line) and agglomerate collision diameter (thick line) predicted along the burner axis for case 1–5. The hard- and soft-agglomerate regions defined according to the work of Tsantilis and Pratsinis [19]. The hard agglomerate region is indicated for each case by using two vertical lines (beginning point of the region; $d_c/d_p = 1.01$) and ending point of the region; = 99% of final d_p intersected with the relevant thick line. The aggregate formation begins at ~26.6 cm above the burner for case 1 while this position moved ~6 cm closer towards the burner in case 4 and 5. For case 4 and 5 sintering stops at 30.8 cm above the burner while in case 1 stops at 40.5 cm above the burner. The agglomerate size at the end of hard agglomerate region is decreased from 22.47 to 17.02 nm for case 1 and 5, respectively. Higher pressure drop across the nozzle tip increases the velocity and mixing of fuel and oxidant above the burner which lowers the flame height and increases the cooling rate (Fig. 10a, b). Increasing the cooling rate hinders the sintering and accelerates the collision of primary particles which results in bigger soft-agglomerates and smaller primary particle diameters. The primary particle diameter of zirconia nanoparticles decreased from 22.7 to 17.2 nm in case 1 and 4, respectively. The soft-agglomerates increased from 43.2 to 55.6 nm for case 1 and case 5 at 50 cm above the burner. Increasing the pressure from 7 to 10.2 didn't have any effect on the primary particle and hard- and soft-agglomerate diameter due to the same velocity and temperature profiles, shown in Fig. 10a, b. In Fig. 11b, the evolutions of the number of primary particles per aggregate along the burner axis are indicated for case 1–5. Close to the burner exit, the high flame temperatures allows full coalescence ($n_p = 1$) further downstream, the coagulation started to take over the sintering as the temperature steadily decreased. The number of primary particle per agglomerate increased from 3.2 to 8.3 for case 1 and 5 which resulted from smaller primary particles at higher pressure drop.

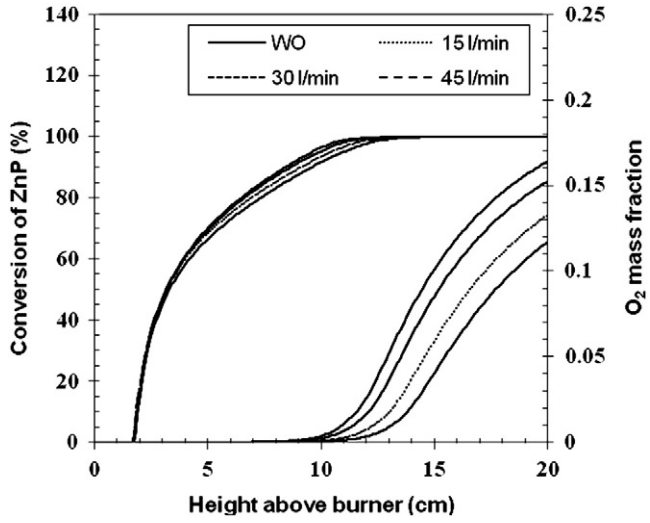

Fig. 13. ZnP Conversion rate (%) for oxygen and ZnP/ethanol flow rates of 70 l/min and 81.1 ml/min without (WO) and with (15–45 l/min) sheath gas flow rate, along with the corresponding oxygen mass fractions above the burner.

Table 2
Operating conditions at different GLFRs.

Flame	A	B	C	D
GLFR	700:1	900:1	1100:1	1300:1
Oxygen flow rate (l/min)	57	73	89	105
ZnP/ethanol feed rate (ml/min)	81.1			
Pressure drop (bar)	7			
Zirconia production (g/h)	300			

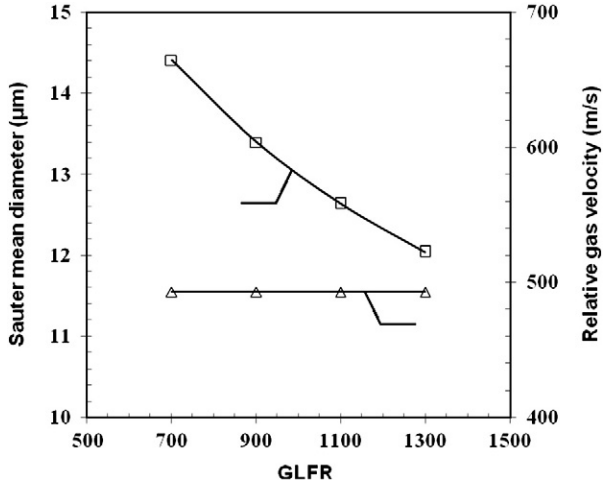

Fig. 15. Sauter mean diameter of ZnP/ethanol droplets at different GLFRs while keeping the relative velocity constant by maintaining the pressure drop at 7 bar.

5.2.2. Effect of sheath gas

Fig. 12 shows the temperature profiles of calculated flames which corresponds to case 4 without (a) and with (b, c, and d) 15, 30, and 45 l/min oxygen sheath flow rate. Initially, the temperature increases as fuel and precursor are consumed, while shortly it decreases rapidly since there is no fuel left to react with the entrapped oxidant. Along the flame axis, it is a little earlier approach towards the high temperature as the sheath flow rate increased from 0 to 45 l/min. This is due to higher available oxidant at the burner exit which contributes to faster combustion of fuel and decomposition of precursor. Fig. 13 shows the centerline ZnP conversion and oxidant mass fraction at above the burner at different sheath gas flow rates. Initially, close to the burner due to high mass fraction of fuel and precursor the mass fraction of oxygen is zero. At a distance of 10 cm above the nozzle exit, the mass fraction of oxygen started to increase. This is the point at which 92 and 97% of the ZnP converted to zirconia at 0 and 45 l/min oxygen sheath flow, respectively. At the same time, the flame is diluted by additional oxygen which increases the gas to particle volume ratio. This would lower the particle collisions and decrease the particle diameter. Making zirconia particles by supplying 0 to 45 oxygen sheath flow decreased the primary particle diameter from 17.2 to 16.8 nm, respectively (see Fig. 14). This shows that the dilution of the sheath gas was not significantly dominant since enough oxygen was already provided to the main flame (70 l/min) by dispersion gas. Since the role of the sheath gas flow is to ensure complete conversion of the precursor, stabilize the fluid flow and decreasing the particle diameter by increasing the dilution and decreasing the particle collisions, it was found that there won't be any need for additional sheath flow by choosing the right amount of dispersion gas for the main flame (Gas to Liquid Mass Ratio (GLMR) > 1.3). This is in agreement with the FSP studies at high production rates, when an increase of GLMR above 1.2 had a minimal effect on the primary particle diameter of SiO_2 [50].

5.2.3. Effect of gas to liquid volume ratio

Gas to Liquid Flow Ratio (GLFR) was varied at variable nozzle discharge section, so to keep the pressure drop constant across the nozzle (operating conditions as in Table 2). Fig. 15 shows the sauter mean diameter of ZnP/ethanol droplets as a function of GLFR and relative velocity of gas and droplets at zirconia production of 300 g/h using 0.5 M ZnP in ethanol. In this study the pressure drop for all flames (A–D) was kept constant at 7 bar which results in a supersonic regime (~490 m/s) at the dispersion gas exit. As the GLFR increased from 700 to 1300, the initial droplet size decreased from 14.4 to 12.04 μm. In general, the droplet size is directly proportional to mixture liquid viscosity and surface tension, and inversely proportional to GLMR and the relative velocity between oxidant and mixture liquid [49]. The mass ratio of oxidant to mixture liquid is deemed to be the dominant factor reducing the droplet size since the rest of

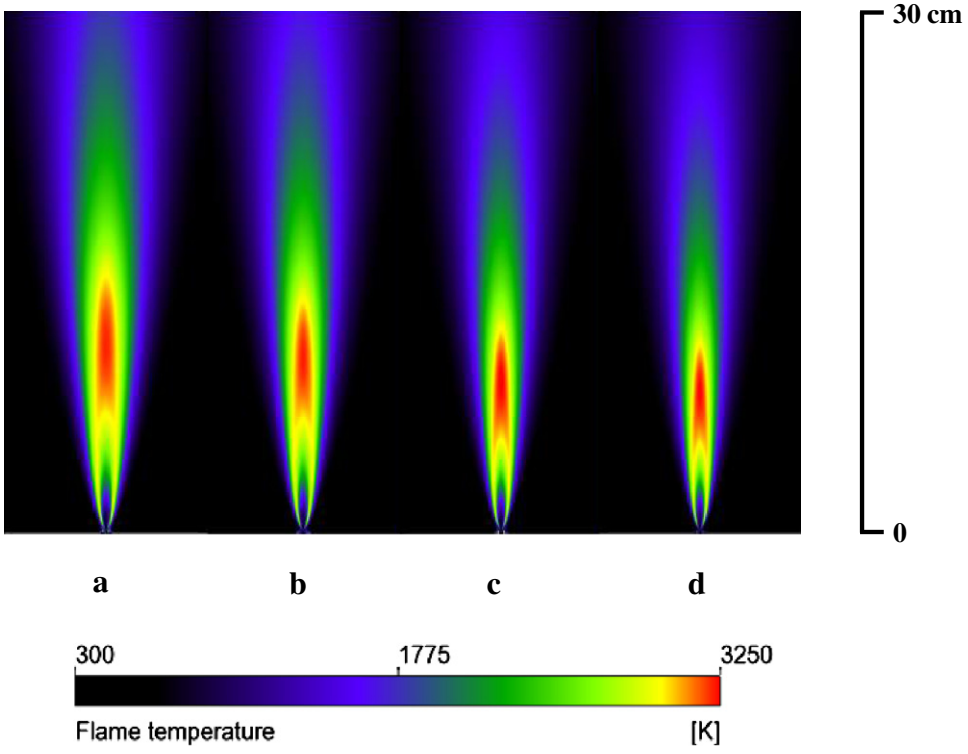

Fig. 16. Predicted flame temperature distribution at different GLFRs (a) 700, (b) 900, (c) 1100, and (d) 1300.

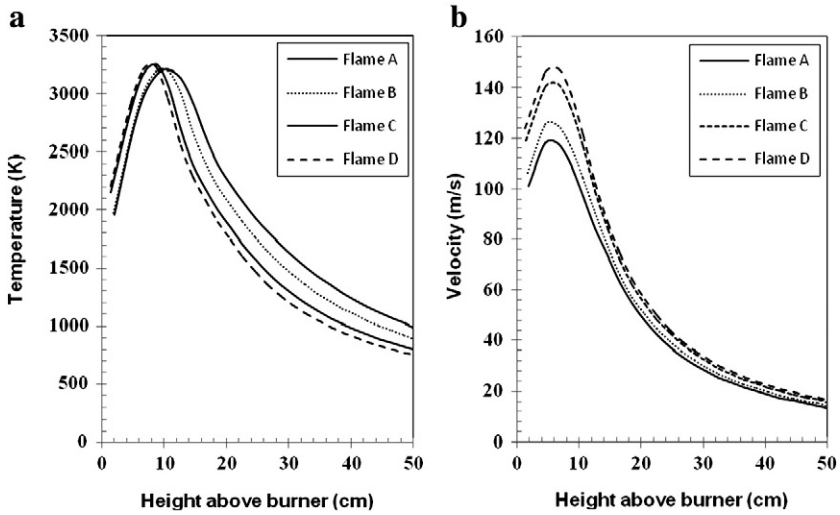

Fig. 17. Simulated center axis (a) temperature and (b) gas velocity profiles at above the burner at different GLFRs.

parameters were kept constant. Increasing the GLFR from 700 to 1300 increased the GLMR by a factor 2. The value of GLFR also affects the flame structure that plays an important role in the determination of particle size during FSP. In order to investigate the variation of the flame structures at different GLFRs, the flame temperature distributions were plotted as shown in Fig. 16. It can be seen that the high GLFR led to shorter flame height and smaller flame region. The spray flame height decreased from 33 to 24 cm as GLFR increased from 700 to 1300. Increasing the GLFR also resulted in steeper drop of temperature downstream of the burner due to higher rate of mixing with excess oxygen (Fig. 17a). Since the pressure drop was kept constant at 7 bar, the flame velocity is proportion to the GLFR. Higher oxidant flow rate intensifies the fuel-oxygen mixing and increases the burning rate of ethanol/ZP droplets which brings the reaction zone closer to the nozzle exit (Fig. 17b) and results in a higher peak velocity. The peak velocity increased from 118 to 148 m/s when the GLFR was increased from 700 (Flame A) to 1300 (Flame D). The expansion of velocity can be explained by the evaporation and combustion of ethanol/ZP droplets and downstream of the burner the velocity decreases with height, since more ambient air is entrained, which has lower momentum and cools the flame. The reaction rates of ZnP molecules are directly depend on the flame temperature and gas velocity distribution. Fig. 18 shows the mass fraction of ZnP for different GLFRs as shown in Table 2. Increasing the GLFR leads to an earlier decomposition of precursor above the burner, which decreases the flame height (Fig. 16). This is strongly affecting the formation and growth of particle since earlier precursor decomposition lowers the flame height and consequently decreases the residence time of particles inside the high temperature zone of the flame which decreases the sintering and growth of particles. Fig. 19a shows the evolution of primary particle and agglomerate collision diameter as a function of GLFR for Flame A–D. In particular, as the GLFR increased from 700 to 1300, primary particle diameter decreased from 18.2 to nearly 15.5 nm. The region of hard agglomerate formation decreased by the order of 1.75 magnitudes when GLFR increased from 700 to 1300. Therefore, the GLFR is strongly affecting the final primary particle size and specially the hard-agglomerate region. The soft-agglomerate diameter is increased from 47.7 to 69.4 nm for Flame A and D at 50 cm above the burner. Due to a very high temperature zone (>2000 K) close to the burner exit as shown in Fig. 17a, only sintering dominates the particle evolution in this region while downstream of the burner the coagulation takes over and stops the evolution of primary particle size. This can be seen from Fig. 19b which shows the number of primary particles per agglomerate for all the flame configurations are 1 np to the beginning of hard agglomerate region and increases according the cooling rate. The number of primary particles per agglomerate is increased from 5.7 to 14.8 due to the higher coagulation which resulted from higher cooling rate at higher GLFR.

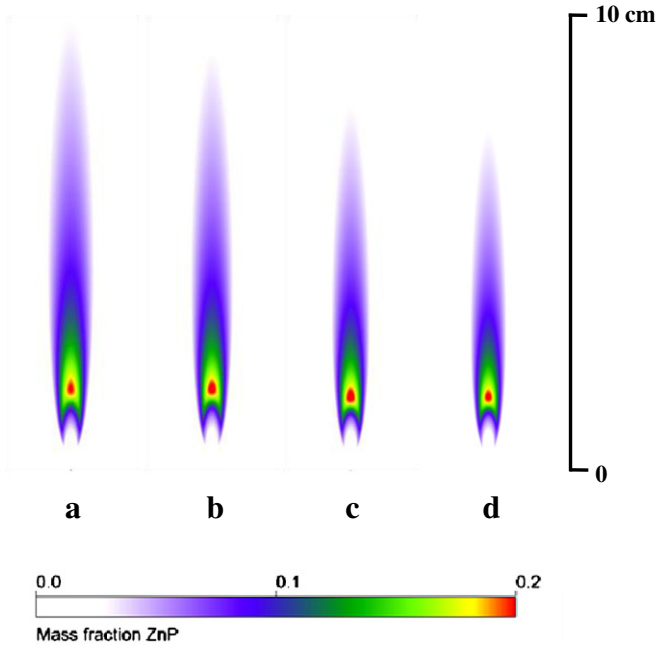

Fig. 18. The mass fraction of the ZnP at different GLFRs.

5.2.4. Effect of production rate

The previous sections showed that the controlled synthesis of 300 g/h zirconia powders via the FSP of 0.5 M ZnP in ethanol can be produced by adjusting the pressure drop, GLFR and without any need to have an additional sheath gas. To study the behavior of the spray flames on the size of primary zirconia particles at different production rates using 0.5 M ZnP in ethanol, the operating conditions of Flame D in the previous section (which is yielded to particle size of 15.5 nm at 300 g/h) is chosen to be tested at lower and higher production rate (Operating conditions as in Table 3). Fig. 20a, b shows the temperature and velocity profiles of 0.5 M ZnP in ethanol solutions producing zirconia at 200, 300 and 400 g/h by applying 7 bar pressure drop to the dispersion gas, keeping the GLFR constant at

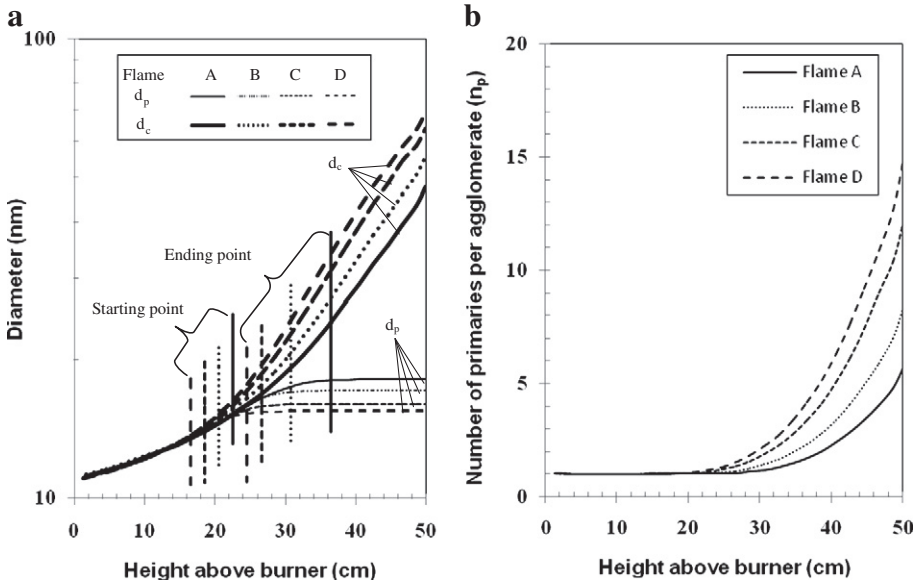

Fig. 19. Evolution of zirconia (a) primary particle (d_p) and agglomerate collision (d_c) diameter, and (b) number of primary particles per agglomerate predicted by the proposed model at different GLFRs.

1300 and without applying any sheath gas. The droplet size was ~12 μm for all the production rates since the GLFR, exit gas velocity and liquid properties kept constant. The spray flame height increases from 20 to 27.5 cm when increasing the production rate from 200 to 400 g/h. This is due to higher supplied fuel energy which prolongs the time for fuel combustion resulting in longer flames. Since the pressure drop and GLFR kept constant, the peak flame velocity is the same (~148 m/s) for all production rates but the position of the peak point above the burner is slightly higher for higher production rate. This is because higher ZnP/ethanol feed rate delays the evaporation of solution and expansion of gas volume after combustion. Fig. 21 shows the particle size is constant while the production rate is increased from 200 to 400 g/h. This phenomenon is due to the constant GLFR and pressure drop which created a constant residence time for zirconia particles in high temperatures at any production rates. The longer flame height at higher production rates theoretically should increase the sintering rate of particles and increase the primary particle diameter but at the same time the flame velocity increased which decreased the time that particles spent at the high temperature zone in the FSP flame which decreased the sintering rate and that is the reason why the primary particle diameter kept ~15.5 nm even at higher production rate. This is a very important feature for scaling-up to industrial production rate.

Table 3
Operating conditions at different production rates.

Zirconia production (g/h)	200	300	400
GLFR	1300:1		
Pressure drop (bar)	7		
Oxygen flow rate (l/min)	70	105	141
ZnP/ethanol feed rate (ml/min)	54.1	81.1	108.1

5.2.5. Effect of precursor concentration

In order to achieve high reactor volume yields at lower production cost, the industrial aerosol reactors should operate at highest possible precursor concentrations. Fig. 22 shows the predicted droplet size as a function of precursor concentration at constant pressure drop (7 bar) and liquid (81.1 ml/min) and dispersion gas (105 l/min) flow rates. Increasing the precursor concentration from 0.5 to 2 M increased

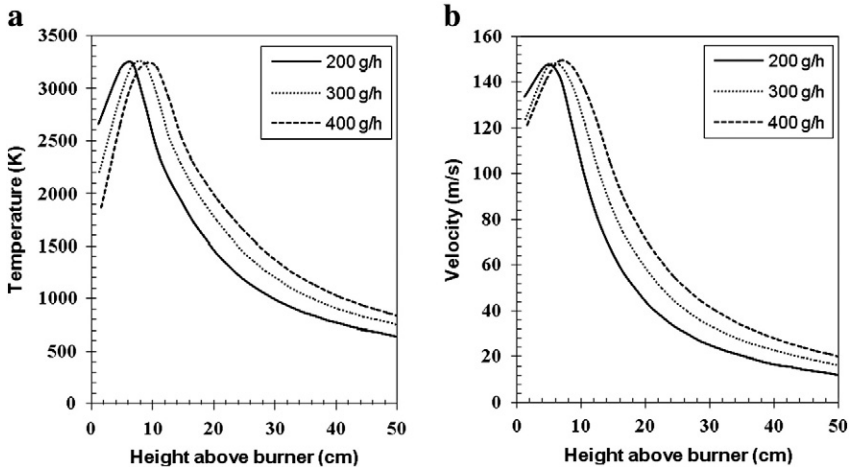

Fig. 20. Simulated center axis (a) temperature and (b) gas velocity profiles at different production rates by keeping the pressure drop and GLFR constant at 7 bar and 1300, respectively.

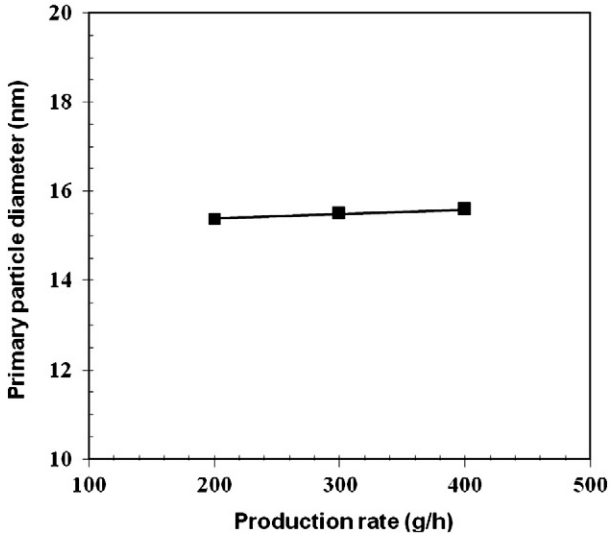

Fig. 21. Effect of the production rate on the predicted primary particle diameters at constant pressure drop and GLFR.

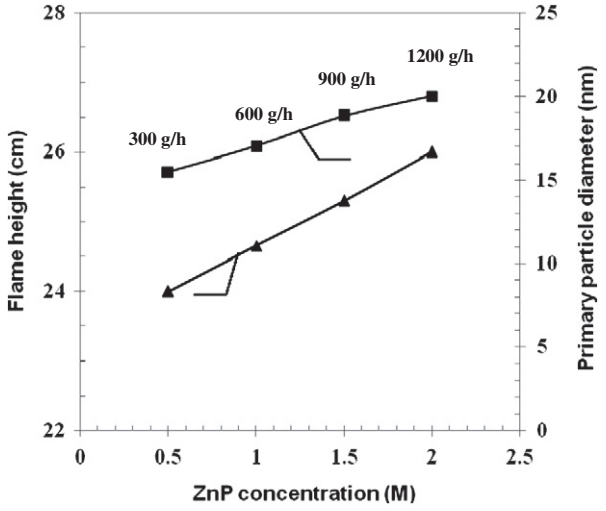

Fig. 23. Primary particle diameter and flame height as a function of precursor concentration.

the droplet size by a factor of 3. Since the relative velocity and GLFR were kept constant, this is a direct result of mixture physical properties which was changed at higher precursor concentration. Increasing precursor concentration from 0.5 to 2 M, increased the viscosity and surface tension from 1.54 to 29 mPa s and 22.7 to 25.6 mN/m, respectively (see Fig. 3a, b). Assuming an ideal mixture, the mixture density also increased from 0.846 to 1.017 g/cm^3 as the ZnP concentration increased from 0.5 to 2 M. Increasing the droplet size at higher precursor concentration increases the residence time for droplets to evaporate which delays the decomposition of precursor and increases the flame height. Fig. 23 shows the flame height and primary particle diameter as a function of precursor concentration. The flame height is increased roughly with an increment of 0.65 cm at each 0.5 M increment. Increasing the precursor concentration results in higher enthalpy content for the flame, prolongs the combustion and increases the particle sintering resulting in the formation of larger primary particles. This is in an agreement with the work of Mueller et al. [10,11] which observed the increase in flame height when they doubled the precursor concentration at fixed liquid and dispersion gas flow rate. Increasing the precursor concentration from 0.5 to 2 M continuously increased the primary particle diameter from 15.5 to 20 nm. This increase for primary particle diameter was expected since the higher precursor concentration will result in a, higher particle concentration which increases the frequency of particle collision and therefore enhances the growth of primary particle especially at higher temperatures (>2000 K). These results are in agreement with FSP studies at high production rate, where an increase of precursor concentration increased the primary particle diameter of silica [50] and zirconia [11].

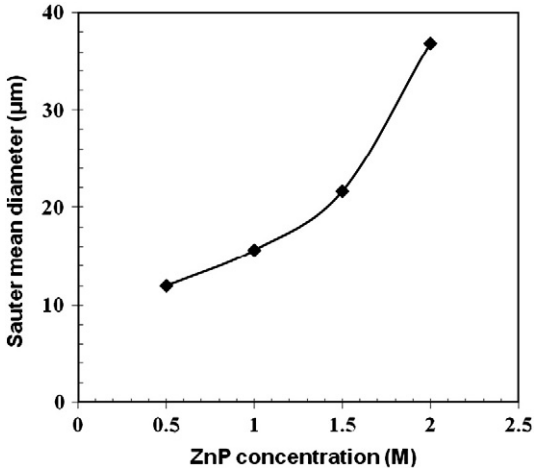

Fig. 22. Sauter mean diameter of ZnP/ethanol droplets at different precursor concentrations.

6. Conclusion

A systematic investigation of synthesis of zirconia nanoparticles at production rates up to 1.2 kg/h was performed using a coupled CFD-monodisperse aerosol model. The model was validated with published experimental data for zirconia nanoparticles synthesis [10–13] using different precursor concentrations and production rates. The effects of processing parameters on the spray flame structure and product particle characteristics were investigated. It was shown how the primary particle diameter can be closely controlled at ~15.5 nm in all production rates by creating a constant residence time for zirconia particles at high temperatures through the constant GLFR and pressure drop using 0.5 M ZnP in ethanol. At higher precursor concentration, the primary particle diameter grew to 20 nm since higher particle concentration increased the coagulation and therefore enhanced the growth of primary particle at above the burner. The framework of current investigation on 0.5 M ZnP in ethanol can be applied to higher precursor concentration in order to keep the particle size constant even under those conditions.

Notation

a	absorption coefficient, 1/m
a_1	constant in SST k–ω model, $a_1 = 0.31$
a^*	coefficient in SST k–ω model
A_d	surface area of the droplet, m^2
c_p	specific heat capacity, J kg^{-1} K^{-1}
C_D	drag coefficient
d_0	orifice diameter, m
d_d	droplet diameter, m
$D_{i,m}$	diffusion coefficient of vapor in the bulk, m^2 s^{-1}
E	total enthalpy, J kg^{-1}
e	sensible enthalpy, J kg^{-1}
F_2	blending function
g_i	i component of gravitational acceleration, m^2 s^{-1}
$\mathbf{h}$	Convective heat transfer coefficient, W m^{-2} K^{-1}
$\mathbf{h}_{v,\,i}$	latent heat of vaporization, J kg^{-1}

J	diffusion flux
k	kinetic energy, $m^2\ s^{-2}$
K	thermal conductivity, $W\ m^{-1}\ K^{-1}$
K_∞	thermal conductivity of continuous phase, $W\ m^{-1}\ K^{-1}$
m	mass, kg
$\dot{m}$	mass flow rate, $kg\ s^{-1}$
n	refractive index
p	pressure, Pa
Pr	Prandtl number
R	Universal gas constant, $J\ mol^{-1}\ K^{-1}$
Re	relative Reynolds number
Re_d	Reynolds number based on droplet diameter
s	path length, m
$\vec{s}$,	direction vector
$\vec{s}$	scattering direction vector
S	source term
Sc	Schmidt number
t	time, s
T	temperature, K
u	velocity, $m\ s^{-1}$
We	Weber number

Greek letters

δ	Kronecker symbol
ε_d	droplet emissivity
ϑ	strain rate magnitude
μ	dynamic viscosity, $kg\ m^{-1}\ s^{-1}$
ρ	density, $kg\ m^{-3}$
σ	Stefan–Boltzmann constant, $W\ m^{-2}\ K^{-4}$
σ_k	turbulent Prandtl number for k
σ_s	scattering coefficient, 1/m
σ_ω	turbulent Prandtl number for ω
τ	deviatoric stress tensor
ω	specific dissipation rate, s^{-1}
Φ	phase function
Ω'	solid angle

Subscript

eff	effective value in reference to the addition of turbulent and non-turbulent contribution of a variable
d	droplet
g	gas
i, j	co-ordinate indices
k	kinetic energy
l	liquid
mix	mixture
R	radiation
sin	sintering
t	turbulent

Acknowledgments

This work was supported by the European Community's Seventh Framework Programme under grant no. CP-FP 228885-2.

References

[1] T. Chraska, A.H. King, C.C. Berndt, On the size-dependent phase transformation in nanoparticulate zirconia, Materials Science and Engineering 286 (2000) 169–178.
[2] N. Miura, H. Kurosawa, M. Hasei, G. Lu, N. Yamazoe, Stabilized zirconia-based sensor using oxide electrode for detection of NO_x in high-temperature combustion-exhausts, Solid State Ionics 86–88 (1996) 1069–1073, (part 2).
[3] H.A. Mcleod, Thin Film Optical Filters. , 2nd Adam Hilger Ltd., Bristol, 1986.
[4] J.H. Shim, C. Chao, H. Huang, F.B. Prinz, Atomic layer deposition of yttria-stabilized zirconia for solid oxide fuel cells, Chemistry of Materials 19 (2007) 3850–3854.
[5] V. Parvulescu, S. Coman, P. Grange, V.I. Parvulescu, Preparation and characterization of sulfated zirconia catalysts obtained via various procedures, Applied Catalysis 176 (1999) 27–43.
[6] Z. Mutasim, W. Brentnall, Thermal barrier coatings for industrial gas turbine applications: an industrial note, Journal of Thermal Spray Technology 6 (1997) 105–108.
[7] M. Guazzato, M. Albakry, S.P. Ringer, M.V. Swain, Strength, fracture toughness and microstructure of a selection of all-ceramic materials. Part II. Zirconia-based dental ceramics, Dental Materials 20 (2004) 449–456.
[8] J. Livage, The gel route to transition metal oxides, Journal of Solid State Chemistry 64 (1986) 322–330.
[9] V.V. Srdic, M. Winterer, H. Hahn, Sintering behavior of nanocrystalline zirconia prepared by chemical vapor synthesis, Journal of the American Ceramic Society 83 (2000) 729–736.
[10] R. Mueller, R. Jossen, H.K. Kammler, S.E. Pratsinis, M.K. Akhtar, Growth of zirconia particles made by flame spray pyrolysis, AICHE Journal 50 (2004) 3085–3094.
[11] R. Mueller, R. Jossen, S.E. Pratsinis, M. Watson, M.K. Akhtar, Zirconia nanoparticles made in spray flames at high production rates, Journal of the American Ceramic Society 87 (2004) 197–202.
[12] M.C. Heine, S.E. Pratsinis, Droplet and particle dynamics during flame spray synthesis of nanoparticles, Industrial and Engineering Chemistry Research 44 (2005) 6222–6232.
[13] M.C. Heine, L. Madler, R. Jossen, S.E. Pratsinis, Direct measurement of entrainment during nanoparticle synthesis in spray flames, Combustion and Flame 144 (2006) 809–820.
[14] K.A. Kusters, S.E. Pratsinis, Strategies for control of ceramic powder synthesis by gas-to-particle conversion, Powder Technology 82 (1995) 79–91.
[15] S.E. Pratsinis, S. Vemury, Particle formation in gases: a review, Powder Technology 88 (1996) 267–273.
[16] S.E. Pratsinis, Flame aerosol synthesis of ceramic powders, Progress in Energy and Combustion Science 4 (1998) 197–219.
[17] J. Karthikeyan, C.C. Berndt, J. Tikkanen, J.Y. Wang, A.H. King, H. Herman, Nanomaterial powders and deposits prepared by flame spray processing of liquid precursors, Nanostructured Materials 8 (1997) 61–74.
[18] L. Madler, S.E. Pratsinis, Bismuth oxide nanoparticles by flame spray pyrolysis, Journal of the American Ceramic Society 87 (2002) 1713–1718.
[19] S. Tsantilis, S.E. Pratsinis, Soft- and hard-agglomerate aerosols made at high temperatures, Langmuir 20 (2004) 5933–5939.
[20] A.J. Grohn, B. Buesser, J.K. Jokiniemi, S.E. Pratsinis, Design of turbulent flame aerosol reactors by mixing-limited fluid dynamics, Industrial and Engineering Chemistry Research 50 (2011) 3159–3168.
[21] A.J. Grohn, S.E. Pratsinis, K. Wegner, Fluid-particle dynamics during combustion spray aerosol synthesis of ZrO_2, Chemical Engineering Journal 191 (2012) 491–502.
[22] F.E. Kruis, K.A. Kusters, S.E. Pratsinis, B. Scarlett, A simple model for the evolution of the characteristics of aggregate particles undergoing coagulation and sintering, Aerosol Science and Technology 19 (1993) 514–526.
[23] F.R. Menter, Two-equation eddy-viscosity turbulence models for engineering applications, AIAA Journal 32 (1994) 1598–1605.
[24] S. Chandrasekhar, Radiative Transfer, Dover Publications, New York, 1960.
[25] B.F. Magnussen, B.H. Hjertager, On mathematical modeling of turbulent combustion with special emphasis on soot formation and combustion, Symposium (International) on Combustion 16 (1977) 719–729.
[26] S.A. Morsi, A.J. Alexander, An investigation of particle trajectories in two-phase flow systems, Journal of Fluid Mechanics 55 (1972) 193–208.
[27] P. Hutchinson, G.F. Hewitt, Deposition of liquid or solid dispersions from turbulent gas streams: a stochastic model, Chemical Engineering Science 26 (1971) 419–439.
[28] G.A. Kallio, M.W. Reeks, A numerical simulation of particle deposition in turbulent boundary layers, International Journal of Multiphase Flow 15 (1989) 433–446.
[29] M.M. Elkotb, M.A. Madhy, M.E. Montaser, Investigation of external-mixing airblast atomizers, Proceedings of the 2nd International Conference on Liquid Atomization and Sprays, Madison, 1982.
[30] L. Grunberg, A.H. Nissan, Mixture law for viscosity, Nature 164 (1949) 799–800.
[31] M. Tamura, M. Kurata, On the viscosity of binary mixtures of liquids, Bulletin of the Chemical Society of Japan 25 (1952) 32–38.
[32] R.K. Hind, E. McLaughlin, A.R. Ubbelohde, Structure and viscosity of liquids, Transactions of the Faraday Society 56 (1960) 328–330.
[33] S.L. Oswal, H.S. Desai, Studies of viscosity and excess molar volume of binary mixtures. 1. Propylamine + 1-alkanol mixtures at 303.15 and 313.15 K, Fluid Phase Equilibria 149 (1998) 359–376.
[34] N.A. Fuchs, Evaporation and Droplet Growth in Gaseous Media, Pergamon Press, London, 1959.
[35] S.S. Sazhin, Advanced models of fuel droplet heating and evaporation, Progress in Energy and Combustion Science 32 (2006) 162–214.
[36] S.E. Pratsinis, P.T. Spicer, Competition between gas phase and surface oxidation of $TiCl_4$ during synthesis of TiO_2 particles, Chemical Engineering Science 53 (1998) 1861–1868.
[37] T. Johannessen, S.E. Pratsinis, H. Livbjerg, Computational fluid-particle dynamics for the flame synthesis of alumina particles, Chemical Engineering Science 55 (2000) 177–191.
[38] T. Johannessen, S.E. Pratsinis, H. Livbjerg, Computational analysis of coagulation and coalescence in the flame synthesis of titania particles, Powder Technology 118 (2001) 242–250.
[39] W.S. Coblenz, J.M. Dynys, R.M. Cannon, R.L. Coble, Initial stage solid state sintering models. A critical analysis and assessment, Materials Science Research 13 (1980) 141–157.

[40] A. Kobata, K. Kusakabe, S. Morooka, Growth and transformation of TiO_2 crystallites in aerosol reactor, AICHE Journal 37 (1991) 347–359.
[41] U. Brossmann, R. Würschum, U. Södervall, H.E. Schaefer, Oxygen diffusion in ultrafine grained monoclinic ZrO_2, Journal of Applied Physics 85 (1999) 7646–7654.
[42] A. Madeyski, W.W. Smeltzer, Oxygen diffusion in monoclinic zirconia, Materials Research Bulletin 3 (1968) 369–375.
[43] M. Rösner-Kuhn, W.H. Hofmeister, G. Kuppermann, R.J. Bayuzick, M.G. Frohberg, Investigations of the influence of oxygen on the surface tension of zirconium by the oscillating drop technique, Surface Science 443 (1999) 159–164.
[44] T. Seto, A. Hirota, T. Fujimoto, M. Shimada, K. Okuyama, Sintering of polydisperse nanometer-sized agglomerates, Aerosol Science and Technology 27 (1997) 422–438.
[45] G.D. Byrne, Pragmatic experiments with krylov methods in the stiff ODE setting, Computational Ordinary Differential Equations, by J. Gladwell, I. Cash, Oxford University Press, Oxford, 1992, pp. 323–356.
[46] J.P. Van Doormaal, G.D. Raithby, Enhancements of the SIMPLE method for predicting incompressible fluid flows, Numerical Heat Transfer 7 (1984) 147–163.
[47] S. Kouris, C. Panayiotou, Dynamic viscosity of mixtures of benzene, ethanol, and n-heptane at 298.15 K, Journal of Chemical & Engineering Data 34 (1989) 200–203.
[48] G. Vazquez, E. Alvarez, J.M. Navaza, Surface tension of alcohol water + water from 20 to 50 °C, Journal of Chemical and Engineering Data 40 (1995) 611–614.
[49] M. Suyari, A.H. Lefebvre, Drop-size measurements in air-assist swirl atomizer sprays, Central States Combustion Institute Spring Meeting, NASA-Lewis Research Center, Cleveland, OH, USA, 1986.
[50] R. Mueller, L. Madler, S.E. Pratsinis, Nanoparticle synthesis at high production rates by flame spray pyrolysis, Chemical Engineering Science 58 (2003) 1969–1976.